The Astrophysical Journal, 950:20 (10pp), 2023 June 10 https://doi.org/10.3847/1538-4357/accc2c

Dwarf Galaxy Formation with and without Dark Matter–Baryon Streaming Velocities

Anna T. P. Schauer[1], Michael Boylan-Kolchin[1], Katelyn Colston[1], Omid Sameie[1], Volker Bromm[1], James S. Bullock[2], and Andrew Wetzel[3]
[1] Department of Astronomy, University of Texas at Austin, TX 78712, USA; mbk@astro.as.utexas.edu
[2] Department of Physics and Astronomy, University of California, Irvine, CA 92697, USA
[3] Department of Physics and Astronomy, University of California, Davis, CA 95616, USA
Received 2022 October 23; revised 2023 March 23; accepted 2023 April 10; published 2023 June 7

Abstract

We study how supersonic streaming velocities of baryons relative to dark matter—a large-scale effect imprinted at recombination and coherent over ∼3 Mpc scales—affect the formation of dwarf galaxies at $z \gtrsim 5$. We perform cosmological hydrodynamic simulations, including and excluding streaming velocities, in regions centered on halos with $M_{\rm vir}(z=0) \approx 10^{10}\ M_\odot$; the simulations are part of the Feedback In Realistic Environments (FIRE) project and run with FIRE-3 physics. Our simulations comprise many thousands of systems with halo masses between $M_{\rm vir} = 2 \times 10^5\ M_\odot$ and $2 \times 10^9\ M_\odot$ in the redshift range $z = 20$–5. A few hundred of these galaxies form stars and have stellar masses ranging from 100 to $10^7\ M_\odot$. While star formation is globally delayed by approximately 50 Myr in the streaming relative to nonstreaming simulations and the number of luminous galaxies is correspondingly suppressed at high redshift in the streaming runs, these effects decay with time. By $z = 5$, the properties of the simulated galaxies are nearly identical in the streaming versus nonstreaming runs, indicating that any effects of streaming velocities on the properties of galaxies at the mass scale of classical dwarfs and larger do not persist to $z = 0$.

Unified Astronomy Thesaurus concepts: Population III stars (1285); Dwarf galaxies (416); Early universe (435); Primordial galaxies (1293)

1. Introduction

The high-redshift universe is a transformative time in cosmic history studied by numerous numerical simulations, leveraging a broad array of computational methodologies (e.g., Bromm et al. 2002; Yoshida et al. 2003; Clark et al. 2011; Wise et al. 2012; Hirano et al. 2018). With structure formation just starting out, dark matter halos are generally much smaller and very filamentary (Sasaki et al. 2014). Without metals, gas cooling proceeds via hydrogen, helium, and their isotopes and molecules, with molecular hydrogen being the dominant coolant before metal enrichment takes place (Glover 2013).

However, one significant effect that is important for the infall of baryons into low-mass halos at high redshift was discovered less than 15 yr ago (Tseliakhovich & Hirata 2010) and has not been explored in nearly the same detail: there are "streaming velocities" of baryons relative to dark matter that are sourced by acoustic oscillations and imprinted at recombination ($z \sim 1100$). This offset velocity is Gaussian, and the speed of baryons relative to dark matter at any point therefore follows a Maxwell–Boltzmann distribution across large scales in the universe that is coherent on scales smaller than ∼3 Mpc (comoving) and correlated over scales comparable to the acoustic horizon of ∼150 comoving Mpc (see, e.g., Fialkov 2014, for a review).

The rms amplitude of this streaming velocity $v_{\rm bc}$ between baryons and cold dark matter is $\sigma_{\rm bc} \approx 30\ {\rm km\ s^{-1}}$ at recombination. Like all peculiar velocities, it decays as the universe expands as $v_{\rm bc}(z) \propto v_{\rm bc}(z=1090)(1+z)$, but it still plays a significant role in the formation of the first stars. Studies have shown that minihalos, the formation sites of Population III (Pop III) stars, have a smaller baryon content when located in a region of the universe with a significant streaming velocity (Naoz et al. 2011, 2012; Richardson et al. 2013; Schauer et al. 2019a; Conaboy et al. 2022). Even more importantly, the minimum halo mass for first star formation increases (Greif et al. 2011; Maio et al. 2011; Stacy et al. 2011; Hirano et al. 2018; Schauer et al. 2019a), an effect that is even stronger than the presence of H_2 dissociating Lyman–Werner radiation (Machacek et al. 2001; Johnson et al. 2008; Hirano et al. 2015), and that leads to overall delayed star formation (Bovy & Dvorkin 2013). Furthermore, streaming velocities might be associated with direct collapse black hole formation at high redshift (Tanaka & Li 2014; Hirano et al. 2017; Schauer et al. 2017). By considering the presence of streaming velocities in the universe, the formation of the very first star in the universe is delayed by $\Delta z \approx 5$ to $z = 65$, based on a statistical calculation by Fialkov et al. (2012).

On a global scale, streaming velocities significantly influence the 21 cm signal of neutral hydrogen during the Dark Ages before reionization (Visbal et al. 2012; Fialkov et al. 2018; Schauer et al. 2019b; Muñoz et al. 2022). The redshift of reionization itself can vary by $\Delta z = 0.05$–0.5, depending on the model for X-ray heating and the detailed timeline of ionizing sources (Park et al. 2021). The signature of the streaming velocity is, however, lost at low redshift: both the power spectrum (Yoo & Seljak 2013) and the three-point correlation function (Slepian et al. 2018) of luminous red galaxies at redshift 0.4–0.7 allow for only a small imprint of the streaming velocity in large-scale structures.

While the effect of streaming velocities on large scales is likely unmeasurable at low redshifts, it is possible that an archaeological imprint might remain in galaxies: if streaming velocities significantly affect early star formation in low-mass halos, present-day dwarf galaxies might retain this signature in their stellar populations. With increasingly high-resolution simulations, it has been found that dwarf galaxies assemble early (Ricotti & Gnedin 2005; Jeon et al. 2017; Fitts et al. 2018). The ability, therefore, of even smaller halos to form stars is critical for the stellar mass content in dwarf galaxies at the epoch of reionization. Investigating how a high-redshift effect influences the first galaxies is a natural first step in connecting the physics of the high-redshift universe with small galaxies in reach of observations. While dwarf galaxies have been studied extensively for many decades with both observations and simulations, there remain important open questions, such as the too-big-to-fail problem (Boylan-Kolchin et al. 2011), the diversity of rotation curves (e.g., Oman et al. 2015; Santos-Santos et al. 2020), or the planes that satellites are found in (Boylan-Kolchin 2021; Pawlowski 2021; for a review see Sales et al. 2022).

In this study, we investigate for the first time the role of streaming velocities in the formation of dwarf galaxies at the epoch of reionization. Specifically, we directly compare global properties, such as star formation history, halo mass function, or metal enrichment, in three FIRE-3 dwarf galaxy simulations with and without steaming velocities. We further investigate the halo properties in all six simulations between redshifts $z = 20$ and $z = 5$. Our paper is structured as follows: We give an overview of the methodology (the simulations, the implementation of the streaming velocity, and our halo selection criteria) in Section 2. We present the results from large scales to small scales and from a global perspective to individual halos in Section 3, before concluding and discussing caveats in Section 4.

2. Methodology

2.1. Simulations

We select three dwarf galaxies from the FIRE (Hopkins et al. 2014, 2018) simulation suite with the latest FIRE-3 physics implemented (Hopkins et al. 2023): m10a, m10i, and m10m (see, e.g., Fitts et al. 2018; Sameie et al. 2022 for previous studies on these galaxies).[4] These are high-resolution zoom-in simulations centered on individual halos of $M_{\rm halo}(z = 0) = 10^{10}\ M_\odot$—hosts of $M_\star(z = 0) \sim 10^6\ M_\odot$ galaxies—in parent volumes of $(25\ \text{comoving Mpc}\ h^{-1})^3$. We focus on the high-redshift evolution of the galaxies between first star formation ($z = 22$–13) and $z = 5$.

The initial conditions for the simulations without streaming velocities follow the standard setup of zoom-in simulations used for a large number of FIRE papers. We specifically consider galaxies m10a, m10i, and m10m out of this FIRE simulation set that is described in Hopkins et al. (2018). We note that the MUSIC (Hahn & Abel 2011) initial conditions generator is not only used for the FIRE simulation suite but also for other cosmological simulations focusing on the early universe, such as the simulations by Jaacks et al. (2019), Skinner & Wise (2020), Abe et al. (2021), Latif et al. (2021), Park et al. (2021), Schauer et al. (2021), Katz et al. (2021), and Lower et al. (2022), to name just a few of the most recent ones.

The FIRE-3 simulations are run with an updated version of the code GIZMO (Hopkins 2015), and use the mesh-free finite mass (MFM) Lagrangian Godunov method. Mass, energy, and momentum are conserved while the spatial scales adapt to resolve the simulation in high resolution. Feedback, such as radiative feedback from stars, stellar winds, or supernova explosions, is part of the standard prescriptions in FIRE. We work with a ΛCDM cosmology and the WMAP parameters from its 7 yr data release (Komatsu et al. 2011) with h=0.71, $\Omega_{\rm m} = 0.296 = 1 - \Omega_\Lambda$, and $\Omega_{\rm b} = 0.0449$. These parameters differ slightly from the most recent results from the Planck collaboration (Planck Collaboration et al. 2020); these differences are unimportant for our purposes.

While the numerical implementation remains largely unchanged from FIRE-2 to FIRE-3, multiple improvements have been made to the code. These updates include a state-of-the-art ionizing UV background that follows Faucher-Giguère (2020), an explicit treatment of cooling in low-temperature, dense ($T < 10^4$ K and $n > 1$ cm^{-3}) gas, and density-independent star formation criteria. The metallicity floor present in previous versions of FIRE has also effectively been removed in FIRE-3, though primordial chemistry is still not treated explicitly, meaning stars formed out of primordial gas follow a normal initial mass function (IMF) with standard yields. For all changes, we refer the reader to Hopkins et al. (2023).

Our simulations are run in high resolution, with a dark matter particle mass of $M_{\rm DM} \sim 2460\ M_\odot$ and an average gas cell mass of $M_{\rm gas} \sim 500\ M_\odot$. The initial conditions are created at redshift $z = 125$, and snapshots are written out at $z = 50$, 40, and 30, followed by outputs with $\Delta z = 1$ until $z = 20$, and then separated by a timescale of $\approx$10 Myr, resulting in 115 snapshots, in total, down to $z = 5$.

2.2. Inclusion of Streaming Velocities

To rerun the same dwarf galaxy simulations, m10a, m10i, and m10m, with the inclusion of streaming velocities, we use the commonly employed "baryons-trace-dark matter" (BTD) approximation (Hirano et al. 2018; Schauer et al. 2021). Streaming velocities are coherent on the Silk damping scale (Silk 1968), with a coherence length of ∼3 cMpc (Tseliakhovich & Hirata 2010). The high-resolution cutout regions for the galaxy simulation have a size of maximally 1.5 cMpc h^{-1} and are therefore smaller than the coherence length. Under the BTD approximation, we can assume that the velocity offset is constant within the cutout region. At the redshift of initialization, $z = 125$, we therefore add an additional constant velocity to all gas particles. We specifically add the velocity in the x-direction, which is an arbitrary choice and does not influence the results. Even though the BTD approximation artificially enhances the gas power spectrum by neglecting the smoothing of the gas distribution between recombination and the redshift of initialization, the effects on a simulation are minor (Park et al. 2020).

The streaming velocity value is chosen to be $1.945\ \sigma_{\rm bc}$, corresponding to 6.75 km s^{-1} at redshift $z = 125$. A streaming velocity of $1.945\ \sigma_{\rm bc}$ or higher is present in 1% of the volume

[4] Like all FIRE simulations, the initial conditions are generated with MUSIC (Hahn & Abel 2011), and the initial condition files can be found at http://www.tapir.caltech.edu/~phopkins/publicICs/. The FIRE simulations assume the same transfer functions for both dark matter and baryons, which can suppress the gas fraction of very small minihalos with masses of $2 \times 10^5\ M_\odot$ by 50% (Naoz et al. 2009, 2011; McQuinn & O'Leary 2012; O'Leary & McQuinn 2012; Naoz et al. 2013; Conaboy et al. 2022).

of the universe. We therefore focus on a rare, but not extremely rare, region of the universe with a large streaming velocity to maximize the effects.[5] Simulations that include streaming velocities are labeled "m10a-vbc," etc., where vbc stands for velocity between baryons and cold dark matter, as commonly used in the literature.

2.3. Halo Selection

Halos are identified using the dark matter halo finder ROCKSTAR (Behroozi et al. 2013). We consider all halos at redshift $z = 5$ that have a mass of at least $10^5\,M_\odot$, corresponding to at least 40 dark matter particles. We also limit our halos to well-resolved ones with at least 99% of the dark matter mass comprised of high-resolution dark matter particles (some halos at the edges of the high-resolution zoom-in region have significant fractions of low-resolution dark matter, and are excluded from this analysis).

We categorize halos into main halos and subhalos: if the center of a halo lies within the virial radius of a more massive halo, it is a subhalo, otherwise, it is a main halo. We compute the virial mass and radius of a halo relative to an overdensity of 200 times the cosmic background density at the given redshift. Gas and stars are attributed to a halo if they lie within its virial radius. Stars further have to be kinematically bound to the halo by having a relative velocity, with respect to the halo center, of less than 2 times the escape velocity. Each star particle is at most associated with one halo, and we attribute it to the smaller halo (subhalo) if the aforementioned conditions are fulfilled by more than one halo. We count a halo as luminous/star-forming if it hosts at least one star particle (so $M_\star \geqslant 430\,M_\odot$).

3. Results

We start our analysis by looking at the large-scale structure of our three simulations and their streaming velocity counterparts (labeled with "vbc"). In Figure 1, we show slices through the high-resolution regions of simulations m10m (top row) and m10m-vbc (bottom row). The baryon density, evolving from redshift $z = 20$ to $z = 5$ from the first to the third panel, shows a similar structure between the streaming and the nonstreaming run. The simulation including the streaming velocity exhibits slightly lower density contrasts and generally a more "washed-out" behavior than the simulation counterpart without a streaming velocity, although this behavior is not very pronounced. This is consistent with the large-scale behavior of high-redshift simulations that focus on first star formation (see, e.g., McQuinn & O'Leary 2012; Schauer et al. 2021).

Stars generally form at the highest densities, which lie at the intersection of filaments. The sites for star formation (indicated by star symbols) are similar between the realizations at redshift $z = 10$. At redshift $z = 5$, star formation is more extended in m10m, leading to a larger ionized region (fourth panel) and more high-temperature gas (fifth panel). We investigate the stochasticity of this behavior in the following sections.

[5] For example, the CEERS JWST survey targets an area of 100 arcmin^2 (Finkelstein et al. 2017) in the high-redshift universe, corresponding to $\sim$800 cMpc^3 at $z = 10$. The probability of finding at least one region with a streaming velocity of $v_{\rm bc} \geqslant 1.945\ \sigma_{\rm bc}$ in this volume is more than 50% at redshift $z = 10$.

3.1. Dark Matter Halos

To directly compare halos in the streaming velocity simulations and their nonstreaming velocity counterparts, we match halos exceeding $2 \times 10^6\ M_\odot\ h^{-1}$ across paired simulations based on the positions and virial radii of the halos: for each halo in the nonstreaming run, we identify its match in the streaming velocity run as the halo that is the closest in terms of distance. To eliminate possible misidentification of a halo that does not have a (spurious) counterpart with a halo far away, we impose the additional criterion that this distance cannot be larger than $\approx$10 comoving kpc between the candidate match in the streaming versus nonstreaming runs. We further restrict the halo pair matches to halos that differ in virial radii by at most 30% to avoid cross-identifying halos and subhalos.

Figure 2 shows two fundamental properties of the halos: their virial mass and their triaxiality $T = (a^2 - b^2)/(a^2 - c^2)$, where $a \geqslant b \geqslant c$ are the primary axes of the halo. The triaxiality determines the shape of the halo from oblate ($T = 0$) to prolate ($T = 1$). We find that streaming and nonstreaming halo pairs mostly follow a 1:1 correlation with some scatter. The scatter is especially high for the triaxiality. These results are in good agreement with, e.g., Druschke et al. (2020) at $z = 15$, who find that, while the shape and mass of the gas are influenced by streaming velocities, the dark matter halo does not change significantly. Druschke et al. (2020) and Chiou et al. (2021) find that the triaxiality of the whole halos spans a wider range of values for nonzero streaming velocity simulations.

The halo mass function remains almost unchanged between the streaming velocity simulations and their nonstreaming counterparts (see Panel (e) in Figures 6 and 7). Only a small fraction of the halos are subhalos; the halo mass function is dominated by main halos in both cases.

3.2. Gas Fraction

We next turn to the gaseous content of the halos in runs with and without streaming velocities. We hereby calculate the gas fraction as the gas mass within the virial radius divided by all mass within the virial radius of a halo.

We see that the gas fractions in the halos in the streaming velocity simulations are strongly reduced compared to the halos of the nonstreaming velocity runs (see Figure 3). In the streaming velocity simulations, the mean gas fraction at redshift $z = 20$ is only 6%, significantly below the mean value of the nonstreaming simulations (13%) and the cosmic mean (16%). In both streaming and nonstreaming simulations, a small number of halos are gas free, as the feedback from the supernova exploding in the halo has removed the gas from the halo. In the streaming simulation, the gas fraction rises with decreasing redshift to $\sim$10%, while the nonstreaming gas fraction stays relatively constant at around 10%–13%. This value is slightly below the cosmic mean value $\Omega_{\rm b}/\Omega_{\rm m} = 0.16$. We find a large variance, with the gas fraction sometimes exceeding the cosmic mean. The gas fraction depends on the exact method for calculating the halo mass. If we take the virial mass determined by ROCKSTAR instead of all mass within the virial radius, we obtain larger gas fractions for both the streaming and nonstreaming simulations by a few percent. The overall trend, however, is unchanged: the gas fraction in streaming simulations is suppressed compared to the nonstreaming simulations. This result is in agreement with the simulations performed by Naoz et al. (2013), who find a sub-

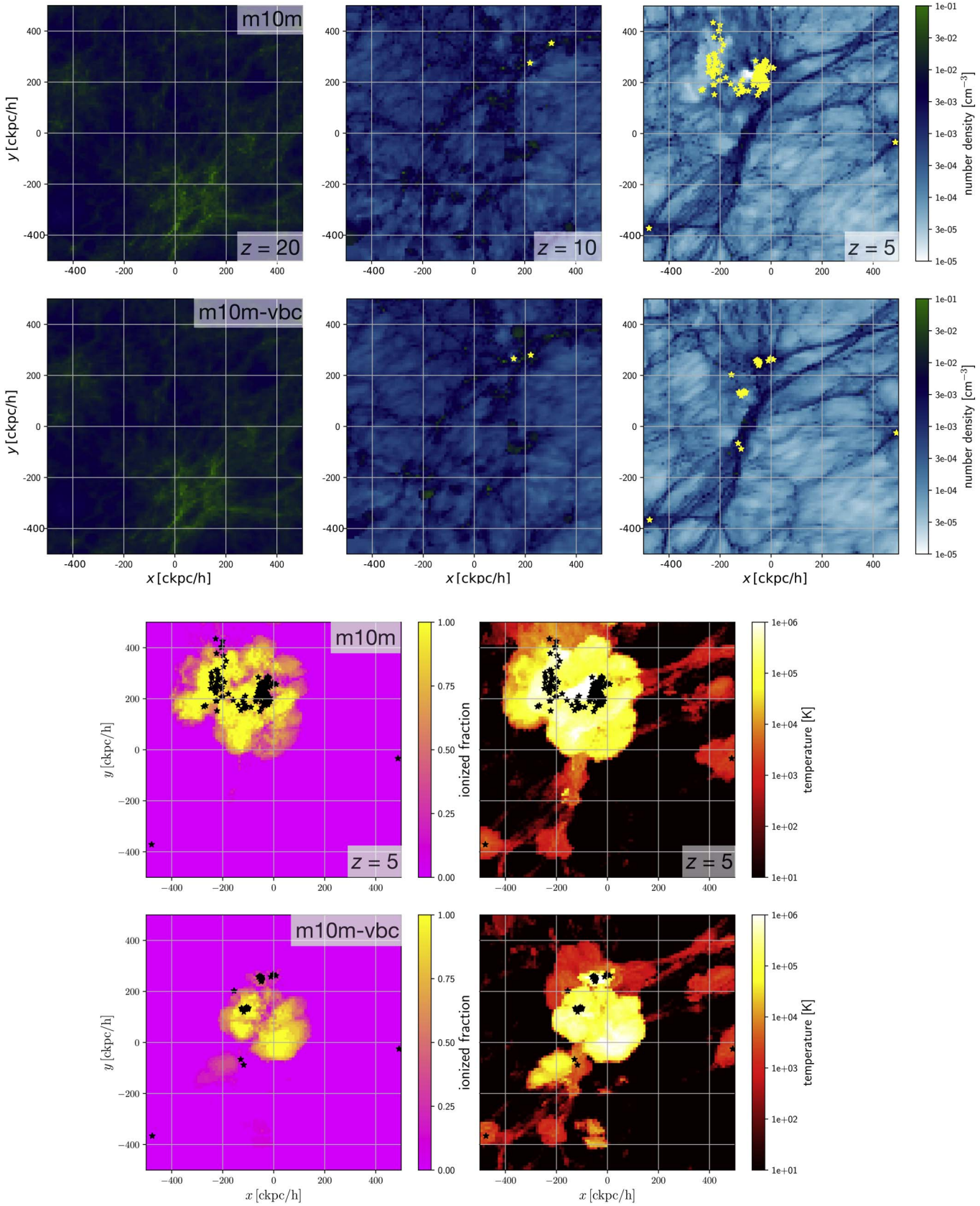

Figure 1. Large-scale slice plots (width 100 ckpc h^{-1}) of the baryon content of simulations m10m (nonstreaming velocities; first and third rows) and m10m-vbc (including streaming velocities; second and fourth rows). The first two rows show the gas number density, where we can see filaments and halos developing over the redshift range from $z = 20$ via $z = 10$ to $z = 5$. Stars that form in the simulation are marked with filled symbols. In the third and fourth rows, we show the ionization fraction and the temperature of the gas at $z = 5$, respectively.

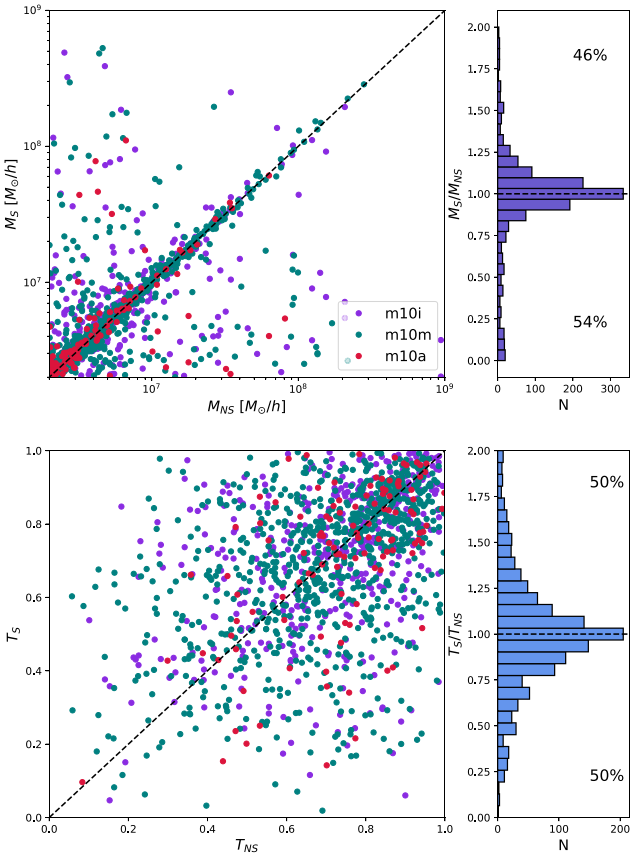

Figure 2. Virial masses (top panels) and triaxialities (bottom panels) for the halos in the simulations with streaming velocities (horizontal axis) and their nonstreaming velocity counterparts (vertical axis) at redshift $z = 5$. The halos follow the 1:1 relation with significant scatter, especially when comparing the triaxialities.

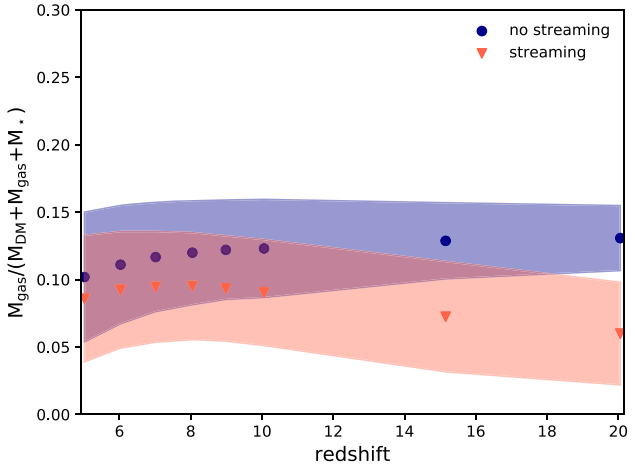

Figure 3. Gas fraction as a function of redshift for the halos in streaming velocity regions (orange) and in nonstreaming velocity regions (blue). We only show the gas fraction in the main halos. Including subhalos leads to much larger, 68%, error bars (shaded regions), with similar mean values (dots/triangles). The gas fraction in streaming velocity halos is smaller than in nonstreaming velocity halos, especially at high redshift.

10% gas fraction in various high-resolution runs at redshift $z = 20$ and below for a streaming velocity of 1.7 σ_{vbc}.

Our initial conditions are set up with MUSIC (Hahn & Abel 2011), and therefore treat the perturbations up to second order. We would like to point out the caveat that the gas fraction changes slightly, especially at redshifts $z > 11$, when considering higher-order effects in the initial condition setup.

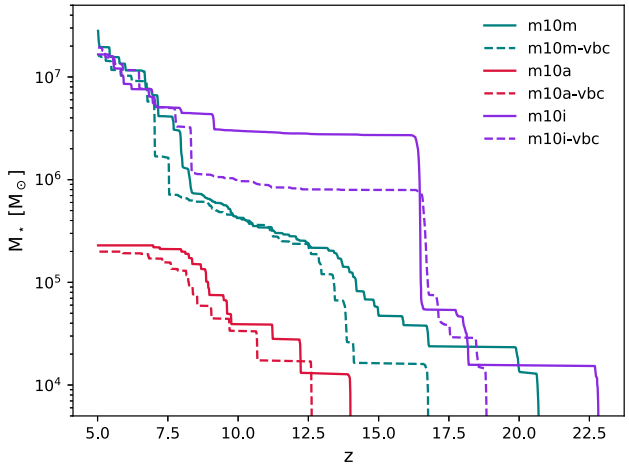

Figure 4. Archaeological star formation histories of all six simulations. We show the stellar mass of all stars present at redshift $z = 5$ as a function of their formation redshift. Stars formed in streaming velocity simulations are shown with dashed lines; stars formed in nonstreaming velocity regions are shown with solid lines. While star formation in streaming velocity simulations is delayed and lags behind the nonstreaming velocity stellar mass counterpart, it is able to catch up to a similar level at redshift $z = 5$.

3.3. Luminous Halos

Globally, star formation is delayed in streaming velocity regions, compared to regions of the universe without a streaming velocity. This can be seen in Figure 4, where we show the cumulative stellar mass at redshift $z = 5$. In all three sets of simulations, the formation of the first star is delayed by approximately 50 Myr (from $z = 14$ in m10a to $z = 12.6$ in m10a-vbc; from $z = 22.9$ in m10i to $z = 18.9$ in m10i-vbc; and from $z = 20.7$ in m10m to $z = 16.8$ in m10m-vbc). In this initial starburst, tens of thousands of solar masses of stars form. In simulations m10i-vbc and m10a-vbc, the initial starburst is more massive than in the nonstreaming velocity counterpart simulations, and the total stellar mass in the streaming velocity simulations exceeds the stellar mass in the nonstreaming velocity simulation for 10–20 Myr. Generally, the simulations without a streaming velocity have a higher stellar mass by a factor of a few, down to redshift $z \approx 8$, when this difference becomes small and merely stochastic. This diminishing difference implies that the star formation rate in the streaming runs is comparable to or greater than that of the nonstreaming runs after the initial onset of star formation, though this effect is relatively modest.

At the same time, the number of luminous halos increases with time. The global delay of star formation in the streaming velocity simulations leads to a global delay in the emergence of galaxies. In Figure 5, we show the number of halos that host stars as a function of redshift for the six individual simulations and the streaming and nonstreaming simulations combined. At the highest redshift, $z = 20$, only simulations m10m and m10i have two and one halo(s) with stars, respectively, while no halo in a streaming velocity simulation has formed stars. At about redshift $z = 10$, there are half as many galaxies in the streaming velocity simulations as in the nonstreaming velocity simulations. This fraction increases until it reaches 90% at redshift $z = 5$.

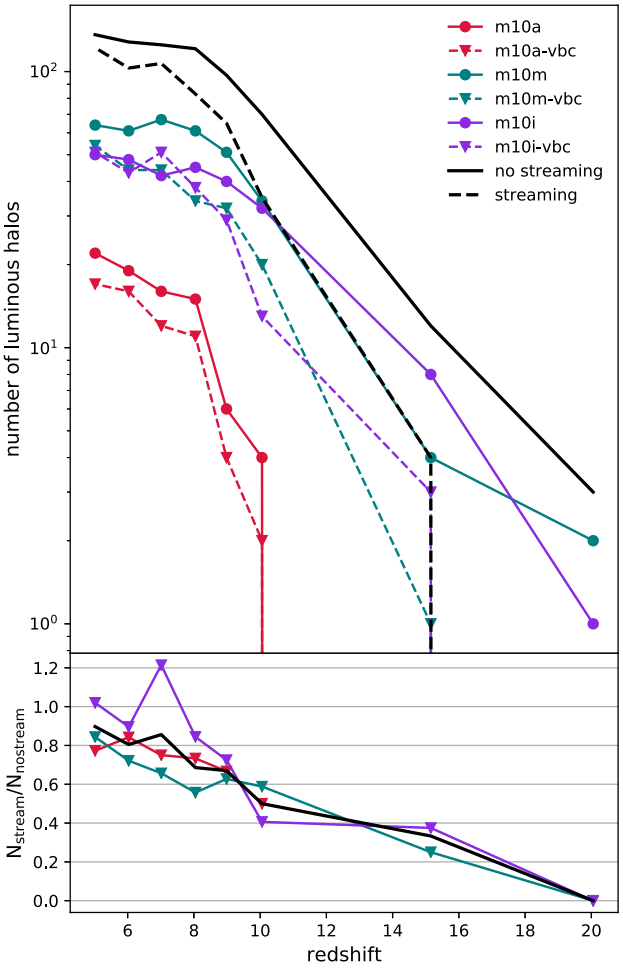

Figure 5. Top: number of luminous halos as a function of redshift for streaming velocity simulations (dashed lines) and nonstreaming velocity simulations (solid lines). In all individual simulations (thin lines), the number of luminous sources is higher for the nonstreaming velocity regions, resulting in the total number of sources (thin lines) also being higher. Bottom: fraction of luminous halos in streaming velocity simulations to those in nonstreaming velocity simulations. The fraction increases from 0 to 90% over the redshift range from $z = 20$ to $z = 5$.

In the next step, we focus on the statistics of the halos at redshifts $z = 10$ and $z = 5$ in Figures 6 and 7. In the bottom left panel, we investigate the difference in halo mass function between the streaming and nonstreaming simulations. The suppression of the halo mass function in our study is comparable to the suppression observed by Lake et al. (2021, their Figure 1), who performed an in-depth analysis of the change in halo mass function for higher-order initial conditions. According to their bottom left panel, the halo mass function is suppressed to 84% (at $2\times10^5\ M_\odot$)–97% (at $10^8\ M_\odot$), when comparing simulations with no and $2\sigma_{\rm vbc}$ streaming runs. At the high-mass end, we have small-number statistics, and it is very unlikely a 3% suppression—as observed by Lake et al. (2021)—will show up in our data. In the three lowest-mass bins, we see a small suppression of halos in the streaming compared to the nonstreaming case, both at $z = 10$ and z = 5.

Most halos form stars during an initial starburst with a total mass of $10^4\ M_\odot$. At redshift $z = 10$ the stellar mass per halo is higher in streaming velocity simulations (panels (a) and (c) of Figure 6), with little correlation to the halo mass. This means that the few halos in a streaming velocity simulation that are able to form stars have an initially larger starburst. At later times, at redshift $z = 5$, the metal-free population is similar in both streaming velocity and nonstreaming velocity runs, with the probability distribution again peaking around $10^4\ M_\odot$ (panels (a) and (c) of Figure 7).

Only a small fraction of halos are metal-enriched, down to redshift $z = 5$ (compare the (b) panels of Figures 7 and 6). This, however, is likely a consequence of not explicitly modeling metal enrichment from Pop III stars, with a top-heavy IMF (e.g., Jeon et al. 2015). At our lowest redshift, we see a weak correlation between halo mass and stellar mass, where more massive halos host larger stellar masses.

Above a halo mass of $10^8\ M_\odot$, almost all halos have formed stars. This fraction decreases rapidly with decreasing halo mass. In an intermediate halo mass range of $10^6\ M_\odot$–$10^8\ M_\odot$, the fraction of nonstreaming halos hosting stars is higher than the fraction of streaming halos hosting stars, with the behavior more visible at earlier times. At small halo masses of a few $10^5\ M_\odot$, the fraction of luminous halos decreases to below (redshift $z = 10$) 0.1%/slightly above (redshift $z = 5$) 0.1%.

Both the mean and median mass of star-forming halos are higher in the case of the halos being embedded in the streaming velocity simulation—by about a factor of 2 at redshift $z = 10$, and by only maximally 10% at redshift $z = 5$. The same is true when focusing on the star-forming main halos only, with the mean and median being of up to a factor of 2 larger at redshift $z = 10$ and of only up to 15% larger at redshift $z = 5$. These values are smaller than the factor of 6 increase reported by Schauer et al. (2021), averaged over a redshift range of $z = 22$ through $z = 14$, and also smaller than the factor of 3 increase in halo mass reported by the early study by Greif et al. (2011) in the redshift range of $z = 30$–15.

The size of the star-forming regions spans several orders of magnitude. We calculate the half-mass radius of stars associated with a halo (see Figure 8) and find them ranging between 1 and 60 pc at redshift $z = 10$. At redshift $z = 5$, this spread is even larger, from subparsec scales to almost 1 kpc. The very small half-mass radii are associated with a small stellar population of around $1000\ M_\odot$, below the mass of a globular cluster. We see little difference in the streaming and the nonstreaming half-mass radii at both redshifts.

4. Summary, Discussion, and Conclusions

In our study, we have examined the effects of streaming velocity on a set of three dwarf galaxy progenitors from the FIRE-3 simulation suite, studying several thousand progenitor halos between the redshift of first star formation down to the epoch of reionization. In agreement with multiple high-redshift studies, we find that the onset of star formation is delayed, by approximately 50 Myr, in all three simulation pairs. The total mass in stars is subsequently smaller, down to a redshift of $z \sim 8$. The number of luminous sources (galaxies inside dark matter halos) in streaming velocity regions versus nonstreaming velocity regions increases from a few percent at redshift $z = 20$ to 50% at $z = 10$, until it almost becomes equal at the lowest redshift probed here ($7 > z > 5$).

At these low redshifts, we also see no significant change in the minimum halo mass for star formation. The reason for this is only partially due to metal enrichment; galaxy formation at lower redshift is increasingly unaffected by the decreasing streaming velocity. We conclude that while streaming velocities significantly affected the high-redshift universe during the Dark Ages, the effects become less important even in small

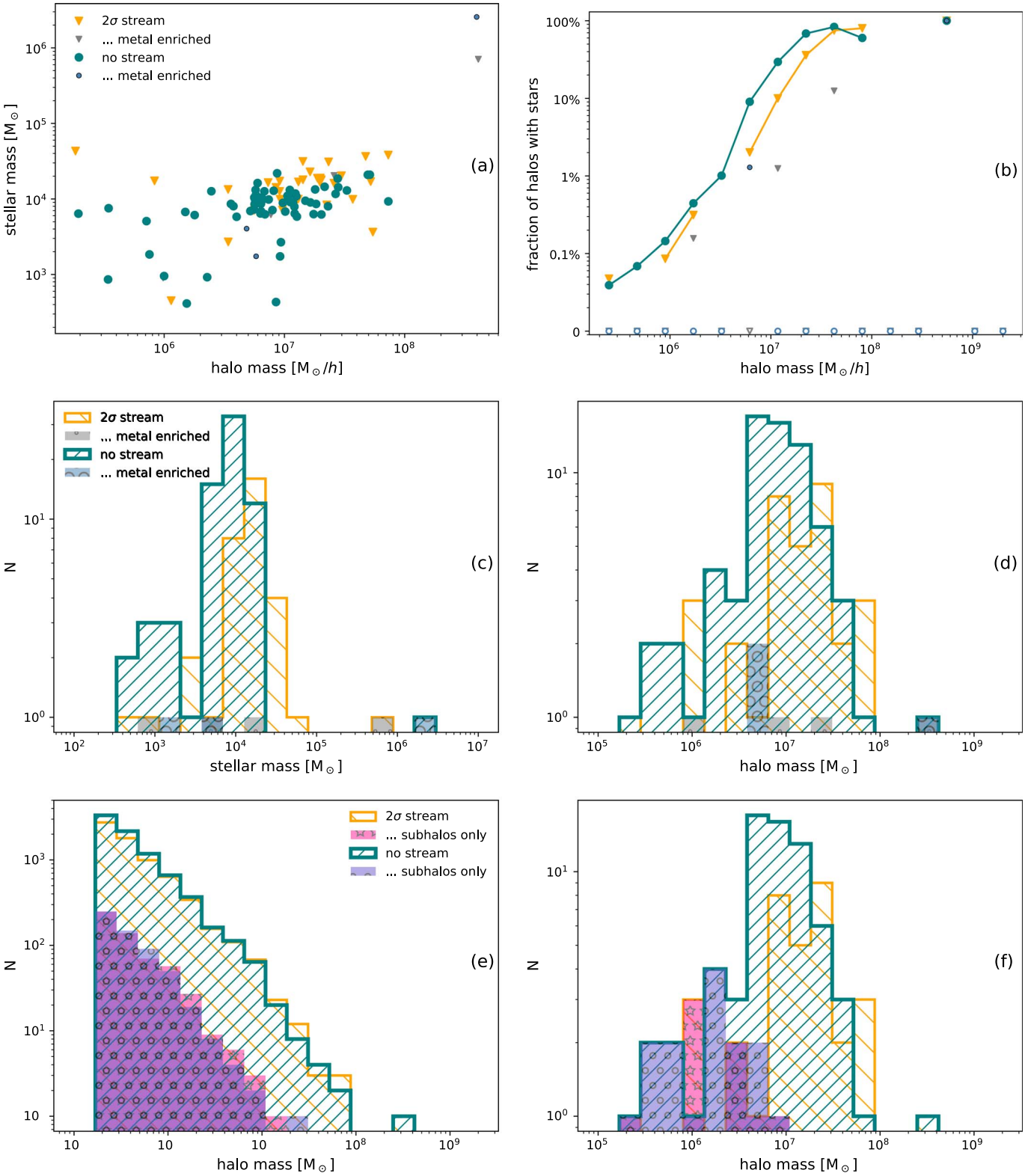

Figure 6. Various halo statistics for redshift $z = 10$. From top left (panel (a)) to bottom right (panel (f)): (a) stellar mass–halo mass relation; (b) fraction of halos that host stars as a function of halo mass; (c) histogram of stellar masses in halos; (d) histogram of halo masses of halos that host stars; (e) histogram of all dark matter halos; (f) histogram of halo masses of halos that host stars. Halos from nonstreaming velocity simulations are shown with teal (points); halos from streaming velocity simulations are shown with yellow (triangles). Panels (a)–(d) distinguish between metal-free (light color) and metal-enriched (gray/black component) stars. Panels (e) and (f) distinguish between all halos and subhalos (pink/purple).

galaxies at the epoch of reionization. Quantities such as the minimum halo mass for star formation, the half-mass radius of the galaxy, or the stellar mass content show very little difference in a region of high-streaming velocity as compared to a region of nonstreaming velocity at redshift $z = 5$. This is consistent with the results from Gutcke et al. (2022), who do

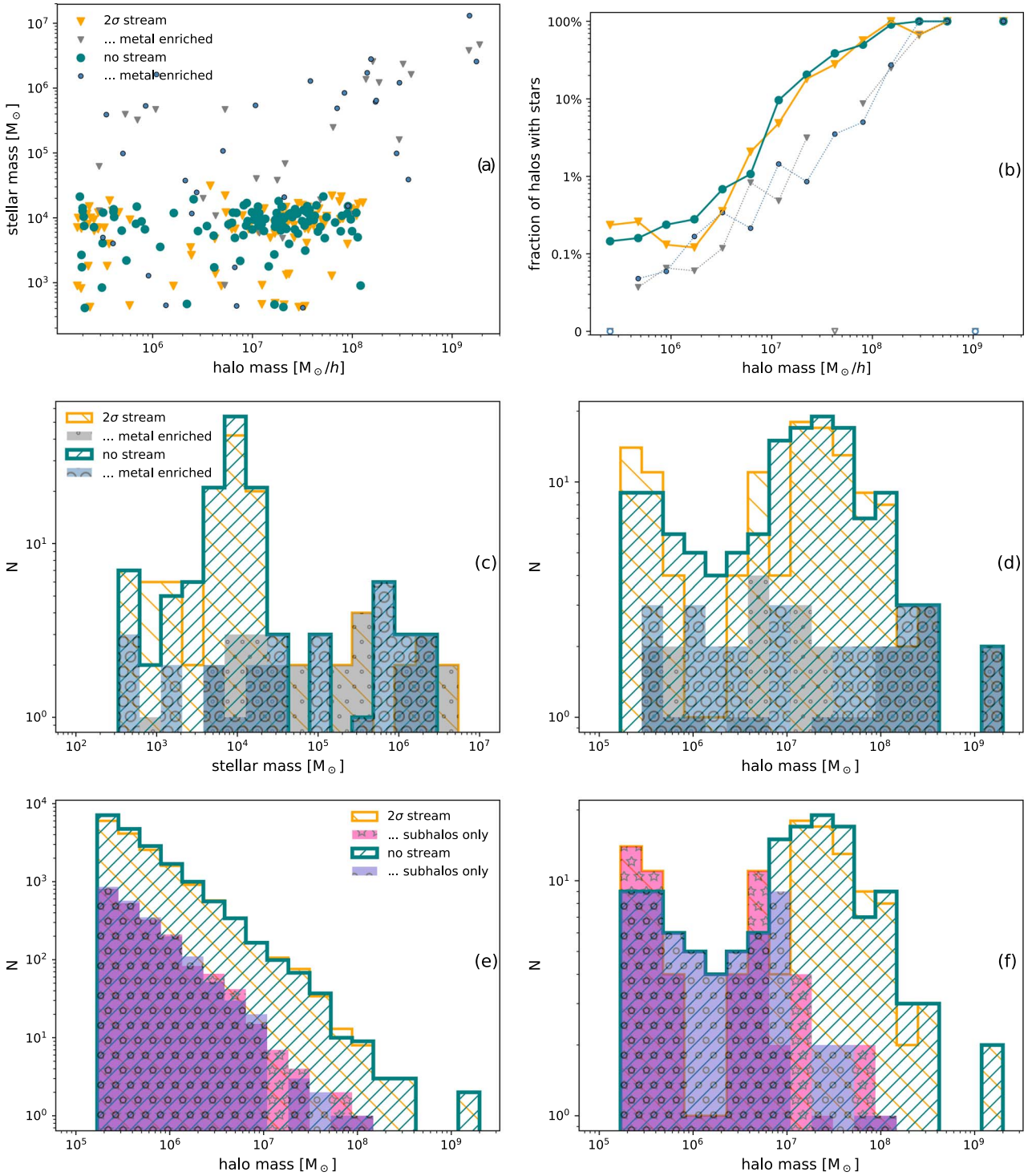

Figure 7. Halo statistics, same as in Figure 6, for redshift $z = 5$.

not include streaming velocities explicitly in their dwarf galaxy simulation but instead alter the halo mass threshold for Pop III star formation—one of the high-redshift effects of streaming velocities. While the onset of first star formation is delayed for a higher halo mass (comparable to the simulations with a streaming velocity), the final stellar and halo masses are not significantly altered.

Our simulations do not self-consistently follow reionization but instead include a global reionization background. This leads to the simulation volume not yet being reionized by redshift 5. Our results are therefore limited to pre-reionization predictions (see, e.g., Milosavljević & Bromm 2014, for assessing this caveat). Our simulations also make the standard assumption that baryons and dark matter share the same transfer function, which can affect the formation of the smallest minihalos (see Section 2). This effect decreases rapidly with halo mass and scale factor, which means it is minimal for all but the first and smallest halos. The adoption of standard FIRE physics and methodologies allows us to connect predictions with streaming velocities directly to the comprehensive

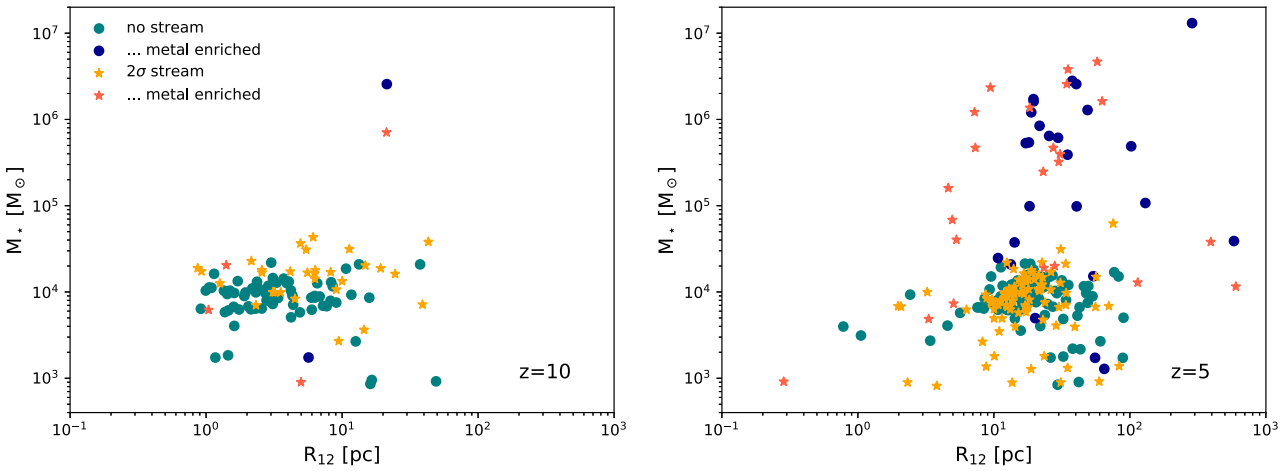

Figure 8. Stellar mass as a function of the half-mass radius of the stars. Halos in nonstreaming velocity regions are shown with blue/teal dots; halos in streaming velocity regions are shown with yellow/orange stars. While the half-mass radii range over several orders of magnitudes, we do not see significant differences between streaming/nonstreaming halos at either redshift $z = 10$ (left panel) or redshift $z = 5$ (right panel). Metal-enriched galaxies have, on average, larger half-mass radii, as multiple star formation events spread the stars over larger radii.

simulation series without streaming velocities that have been widely used and discussed in the literature. This paper serves as an example for other large simulation projects, demonstrating that results at redshifts 5–7 do not heavily depend on the inclusion of streaming velocities.

A detailed study of individual halos requires more resolution elements, especially if kinematic properties such as the spin or the circularity are considered (Sasaki et al. 2014), than we provide with our study. However, other quantities, such as the halo or gas mass, can be estimated sufficiently accurately with a smaller number of particles per halo. For example, the THESAN simulations (Kannan et al. 2022) use a similar threshold of 50 particles/galaxy. Furthermore, the star-forming halos in this study either have a mass larger than $5 \times 10^6\, M_\odot$ or subhalos within a more massive host and are therefore resolved by more than a few hundred particles.

Even though the effects of streaming velocities on properties such as the luminosity function get smaller with redshift, we cannot exclude for certain the possibility of persistent observable features. We run our simulations with standard FIRE-3 physics, which does not follow Pop III star formation explicitly with a network of primordial chemistry and an altered initial mass function for metal-free stars (see, e.g., Jaacks et al. 2019). Different chemical abundance patterns, for example, or different levels of r-process enrichment (Jeon et al. 2021), could be found if distinguishing between Pop III and Pop II star formation and nucleosynthesis (Jeon et al. 2017), possibly allowing us to determine if a first galaxy was born in a region of high or low streaming velocity.

In the future, we plan on including the formation of Pop III stars in the simulation, as carried out in a recent study by Sanati et al. (2023) with the smoothed-particle hydrodynamics (SPH) code GEAR. It will be interesting to see if this result is influenced by pure Pop III star formation since Pop III stars are expected to survive in pristine clumps down to redshift $z = 6$ (Liu & Bromm 2020). Direct modeling of primordial chemistry, such as H_2 or HD formation, will further increase the accuracy of Pop III star formation.

On the observational side, this era of the very first onset of star formation is out of reach for current and upcoming facilities (Jeon & Bromm 2019). A possible exception could be extreme gravitational lensing events, such as the Earendel stellar source (Schauer et al. 2022; Welch et al. 2022), or a potential Pop III star cluster (Vanzella et al. 2020). These single objects, however, fail to characterize the full population of minihalos and small first galaxies. Direct observations of this ultimate high-redshift frontier of star and galaxy formation call for 100 m extraterrestrial telescopes (Angel et al. 2008; Rhodes et al. 2020; Schauer et al. 2020).

We would like to thank Aaron Smith for the helpful comments. M.B.K. acknowledges support from NSF CAREER award AST-1752913; NSF grants AST-1910346 and AST-2108962; NASA grant 80NSSC22K0827; and HST-AR-15809, HST-GO-15658, HST-GO-15901, HST-GO-15902, HST-AR-16159, and HST-GO-16226 from the Space Telescope Science Institute, which is operated by AURA, Inc., under NASA contract NAS5-26555. J.S.B. was supported by NSF grant AST-1910346. A.W. received support from: NSF via CAREER award AST-2045928 and grant AST-2107772; NASA ATP grant 80NSSC20K0513; and HST grants AR-15809, GO-15902, and GO-16273 from STScI.

ORCID iDs

Anna T. P. Schauer https://orcid.org/0000-0002-2220-8086
Michael Boylan-Kolchin https://orcid.org/0000-0002-9604-343X
Omid Sameie https://orcid.org/0000-0003-4394-6085
Volker Bromm https://orcid.org/0000-0003-0212-2979
James S. Bullock https://orcid.org/0000-0003-4298-5082
Andrew Wetzel https://orcid.org/0000-0003-0603-8942

References

Abe, M., Yajima, H., Khochfar, S., Dalla Vecchia, C., & Omukai, K. 2021, MNRAS, 508, 3226
Angel, R., Worden, S. P., Borra, E. F., et al. 2008, ApJ, 680, 1582
Behroozi, P. S., Wechsler, R. H., & Wu, H.-Y. 2013, ApJ, 762, 109
Bovy, J., & Dvorkin, C. 2013, ApJ, 768, 70
Boylan-Kolchin, M. 2021, NatAs, 5, 1188
Boylan-Kolchin, M., Bullock, J. S., & Kaplinghat, M. 2011, MNRAS, 415, L40
Bromm, V., Coppi, P. S., & Larson, R. B. 2002, ApJ, 564, 23
Chiou, Y. S., Naoz, S., Burkhart, B., Marinacci, F., & Vogelsberger, M. 2021, ApJ, 906, 25

Clark, P. C., Glover, S. C. O., Smith, R. J., et al. 2011, Sci, 331, 1040
Conaboy, L., Iliev, I. T., Fialkov, A., Dixon, K. L., & Sullivan, D. 2022, arXiv:2207.11614
Druschke, M., Schauer, A. T. P., Glover, S. C. O., & Klessen, R. S. 2020, MNRAS, 498, 4839
Faucher-Giguère, C.-A. 2020, MNRAS, 493, 1614
Fialkov, A. 2014, IJMPD, 23, 1430017
Fialkov, A., Barkana, R., & Cohen, A. 2018, PhRvL, 121, 011101
Fialkov, A., Barkana, R., Tseliakhovich, D., & Hirata, C. M. 2012, MNRAS, 424, 1335
Finkelstein, S. L., Dickinson, M., Ferguson, H. C., et al. 2017, The Cosmic Evolution Early Release Science (CEERS) Survey, JWST Proposal ID, Cycle 0 Early Release Science, 1345
Fitts, A., Boylan-Kolchin, M., Bullock, J. S., et al. 2018, MNRAS, 479, 319
Glover, S. 2013, in The First Galaxies, Astrophysics and Space Science Library, ed. V. Bromm, B. Mobasher, & T. Wiklind, Vol. 396 (Berlin: Springer), 103
Greif, T. H., White, S. D. M., Klessen, R. S., & Springel, V. 2011, ApJ, 736, 147
Gutcke, T. A., Pakmor, R., Naab, T., & Springel, V. 2022, MNRAS, 513, 1372
Hahn, O., & Abel, T. 2011, MNRAS, 415, 2101
Hirano, S., Hosokawa, T., Yoshida, N., & Kuiper, R. 2017, Sci, 357, 1375
Hirano, S., Hosokawa, T., Yoshida, N., Omukai, K., & Yorke, H. W. 2015, MNRAS, 448, 568
Hirano, S., Yoshida, N., Sakurai, Y., & Fujii, M. S. 2018, ApJ, 855, 17
Hopkins, P. F. 2015, MNRAS, 450, 53
Hopkins, P. F., Kereš, D., Oñorbe, J., et al. 2014, MNRAS, 445, 581
Hopkins, P. F., Wetzel, A., Kereš, D., et al. 2018, MNRAS, 480, 800
Hopkins, P. F., Wetzel, A., Wheeler, C., et al. 2023, MNRAS, 519, 3154
Jaacks, J., Finkelstein, S. L., & Bromm, V. 2019, MNRAS, 488, 2202
Jeon, M., Besla, G., & Bromm, V. 2017, ApJ, 848, 85
Jeon, M., Besla, G., & Bromm, V. 2021, MNRAS, 506, 1850
Jeon, M., & Bromm, V. 2019, MNRAS, 485, 5939
Jeon, M., Bromm, V., Pawlik, A. H., & Milosavljević, M. 2015, MNRAS, 452, 1152
Johnson, J. L., Greif, T. H., & Bromm, V. 2008, MNRAS, 388, 26
Kannan, R., Smith, A., Garaldi, E., et al. 2022, MNRAS, 514, 3857
Katz, H., Martin-Alvarez, S., Rosdahl, J., et al. 2021, MNRAS, 507, 1254
Komatsu, E., Smith, K. M., Dunkley, J., et al. 2011, ApJS, 192, 18
Lake, W., Naoz, S., Chiou, Y. S., et al. 2021, ApJ, 922, 86
Latif, M. A., Khochfar, S., Schleicher, D., & Whalen, D. J. 2021, MNRAS, 508, 1756
Liu, B., & Bromm, V. 2020, MNRAS, 497, 2839
Lower, S., Narayanan, D., Li, Q., & Davé, R. 2022, arXiv:2212.02636
Machacek, M. E., Bryan, G. L., & Abel, T. 2001, ApJ, 548, 509
Maio, U., Koopmans, L. V. E., & Ciardi, B. 2011, MNRAS, 412, L40
McQuinn, M., & O'Leary, R. M. 2012, ApJ, 760, 3
Milosavljević, M., & Bromm, V. 2014, MNRAS, 440, 50
Muñoz, J. B., Qin, Y., Mesinger, A., et al. 2022, MNRAS, 511, 3657
Naoz, S., Barkana, R., & Mesinger, A. 2009, MNRAS, 399, 369
Naoz, S., Yoshida, N., & Barkana, R. 2011, MNRAS, 416, 232
Naoz, S., Yoshida, N., & Gnedin, N. Y. 2012, ApJ, 747, 128
Naoz, S., Yoshida, N., & Gnedin, N. Y. 2013, ApJ, 763, 27
O'Leary, R. M., & McQuinn, M. 2012, ApJ, 760, 4
Oman, K. A., Navarro, J. F., Fattahi, A., et al. 2015, MNRAS, 452, 3650
Park, H., Ahn, K., Yoshida, N., & Hirano, S. 2020, ApJ, 900, 30
Park, H., Shapiro, P. R., Ahn, K., Yoshida, N., & Hirano, S. 2021, ApJ, 908, 96
Park, J., Ricotti, M., & Sugimura, K. 2021, MNRAS, 508, 6176
Pawlowski, M. S. 2021, NatAs, 5, 1185
Planck Collaboration, Aghanim, N., Akrami, Y., et al. 2020, A&A, 641, A6
Rhodes, J. D., Huff, E., Masters, D., & Nierenberg, A. 2020, AJ, 160, 261
Richardson, M. L. A., Scannapieco, E., & Thacker, R. J. 2013, ApJ, 771, 81
Ricotti, M., & Gnedin, N. Y. 2005, ApJ, 629, 259
Sales, L. V., Wetzel, A., & Fattahi, A. 2022, NatAs, 6, 897
Sameie, O., Boylan-Kolchin, M., Hopkins, P. F., et al. 2023, MNRAS, 522, 1800
Sanati, M., Jeanquartier, F., Revaz, Y., & Jablonka, P. 2023, A&A, 669, A94
Santos-Santos, I. M. E., Navarro, J. F., Robertson, A., et al. 2020, MNRAS, 495, 58
Sasaki, M., Clark, P. C., Springel, V., Klessen, R. S., & Glover, S. C. O. 2014, MNRAS, 442, 1942
Schauer, A. T. P., Bromm, V., Drory, N., & Boylan-Kolchin, M. 2022, ApJL, 934, L6
Schauer, A. T. P., Drory, N., & Bromm, V. 2020, ApJ, 904, 145
Schauer, A. T. P., Glover, S. C. O., Klessen, R. S., & Ceverino, D. 2019a, MNRAS, 484, 3510
Schauer, A. T. P., Glover, S. C. O., Klessen, R. S., & Clark, P. 2021, MNRAS, 507, 1775
Schauer, A. T. P., Liu, B., & Bromm, V. 2019b, ApJL, 877, L5
Schauer, A. T. P., Regan, J., Glover, S. C. O., & Klessen, R. S. 2017, MNRAS, 471, 4878
Silk, J. 1968, ApJ, 151, 459
Skinner, D., & Wise, J. H. 2020, MNRAS, 492, 4386
Slepian, Z., Eisenstein, D. J., Blazek, J. A., et al. 2018, MNRAS, 474, 2109
Stacy, A., Bromm, V., & Loeb, A. 2011, ApJL, 730, L1
Tanaka, T. L., & Li, M. 2014, MNRAS, 439, 1092
Tseliakhovich, D., & Hirata, C. 2010, PhRvD, 82, 083520
Vanzella, E., Meneghetti, M., Caminha, G. B., et al. 2020, MNRAS, 494, L81
Visbal, E., Barkana, R., Fialkov, A., Tseliakhovich, D., & Hirata, C. M. 2012, Natur, 487, 70
Welch, B., Coe, D., Diego, J. M., et al. 2022, Natur, 603, 815
Wise, J. H., Abel, T., Turk, M. J., Norman, M. L., & Smith, B. D. 2012, MNRAS, 427, 311
Yoo, J., & Seljak, U. 2013, PhRvD, 88, 103520
Yoshida, N., Abel, T., Hernquist, L., & Sugiyama, N. 2003, ApJ, 592, 645